Applied Physics Express **13**, 065502 (2020)
https://doi.org/10.35848/1882-0786/ab8b6b

LETTER

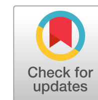

Evolution of implicate order from amorphous to polycrystalline Sn-doped In_2O_3 films determined by in situ two-dimensional X-ray diffraction measurements

Yutaka Furubayashi[1*], Shintaro Kobayashi[2], Makoto Maehara[3], Kazuhiko Ishikawa[2], Katsuhiko Inaba[2], Toshiyuki Sakemi[4], Hisashi Kitami[1,4], and Tetsuya Yamamoto[1]

[1]*Materials Design Center, Research Institute, Kochi University of Technology, Tosayamadacho-Miyanokuchi 185, Kami 782-8502, Japan*
[2]*Rigaku Cooperation, Matsubaracho 3-9-12, Akishima 196-8666, Japan*
[3]*Industrial Equipment Division, Sumitomo Heavy Industries, Ltd., Soubiraki-cho 5-2, Niihama 792-8588, Japan*
[4]*Technology Research Center, Sumitomo Heavy Industries, Ltd., Natsushimacho 19, Yokosuka 237-8555, Japan*

*E-mail: furubayashi.yutaka@kochi-tech.ac.jp

Received April 9, 2020; revised April 16, 2020; accepted April 21, 2020; published online May 4, 2020

We elucidated implicate ordering of amorphous Sn-doped In_2O_3 films grown on glass substrates during the phase transition to polycrystalline by postannealing from room temperature to 300 °C for 55 min. X-ray diffraction with two-dimensional detector revealed the following. First, fine grains are developed. Second, crystallites are grown with (222) preferential orientation associated with growing crystallites along (222) plane. Simultaneously, the alignment between grains is also promoted. Finally, while retaining the alignments among crystallites, long-range ordering was improved within the crystallites. Based on those findings, as a well-defined crystallization temperature, we propose a temperature at which the above-mentioned final stage starts. © 2020 The Japan Society of Applied Physics

The solid-state (or solid-phase) crystallization of amorphous films based on various materials, including silicon,[1,2] metals,[3–5] and TiO_2,[6,7] has attracted considerable interest. Recently, we have reported a very high Hall mobility (μ_H) of 145 cm^2 V^{-1} s^{-1} for transparent conductive cerium–hydrogen co-doped In_2O_3 polycrystalline films obtained by the postannealing of the amorphous phase at 200 °C for 30 min in air.[8] In_2O_3 has a bixbyite crystal structure (space group *Ia*-3, number 206) and has been mostly applied to transparent conducting oxide films.[9–11] Taking into account the high μ_H of amorphous[12] and solid-state-crystallized[8,13] films, the investigation of the effects of solid-state crystallization on the properties of amorphous In_2O_3 (a-In_2O_3) films[14–18] is of fundamental importance. The solid-state-crystallization has been studied in the framework of thermodynamic kinetics, and some theoretical models have been proposed.[1,4,7,14,19] Most reports have focused on time-dependent phenomena of crystallization at a fixed annealing temperature. Note that problems remain with the conventional definition of the "crystallization temperature" (T_{cr}) corresponding to the development of crystallites in amorphous films having lattices without long-range order. In most cases, the crystallization process has been investigated by three different techniques: X-ray diffraction (XRD), transmission electron microscopy, and scanning electron microscopy. T_{cr} has thus been simply regarded as the temperature at which XRD peaks corresponding to the orientation of crystal planes appear.

In this letter, we propose an alternative to the conventional T_{cr}. The two reasons are as following. The first is that the solid-state-crystallization process of this study was carried out through a non-equilibrium process. As illustrated in Fig. 1, as the substrate temperature rises not slowly, we find a difference in temperature between a lower temperature at a film surface (T_{sur}) and a higher temperature at the interface (T_{if}). In case that a plane size of a film is sufficiently larger than a film thickness, heat radiation from surfaces in contact with the air is negligible; a heat at the film surface is closely equal to that at the interface, denoted by Q. In such a case, the entropy at the film surface ($S_{sur} = Q/T_{sur}$) is higher than that at the interface ($S_{it} = Q/T_{if}$). This finding shows that the postannealing process of this study would gives rise to an increase in the entropy in the film; the process suppresses the generation of order of the film. The solid-state crystallization in the non-equilibrium is in essential a competition between the ordering and disordering. The second is that the conventional definition of T_{cr} makes sense in the phenomena of ordering in single crystallite films without grains. Polycrystalline films are composed of grains with grain boundaries between crystallites. In addition, the grain size together with the spatial distribution of the grain boundaries is expected to be one of the dominant factors that determine the electrical behaviors of whole polycrystalline films. These are the motivation for our inquiry into our basic notions of implicate order in polycrystalline films. In this letter, we investigated the dynamics of changes in the microstructure of as-deposited amorphous Sn-doped In_2O_3 (a-ITO) films by increasing the substrate temperature (T), by in situ XRD observation with a two-dimensional (2D) detector.

Conventionally, to observe the dynamics of crystallization, i.e. its time evolution, in situ XRD observation is required. For example, energy-dispersion XRD using cyclotron radiation have been applied to detect electric-voltage-,[20] pressure-,[21] and temperature-[22] induced dynamical phase transitions. 2D detector has recently been utilized for the in situ observation of crystallographic behavior because of its short scanning time. At first, it has been applied for constructing reciprocal space mappings.[23,24] However, recently, the time-dependent evolution of the crystallization of a-In_2O_3 films during annealing isothermally has been monitored using the grazing-incidence wide-angle scattering technique with a 2D detector.[25] This report determined the degree of crystallinity by a quantitative analysis of the time-evolved X-ray scattering patterns. The 2D detector allows us to simultaneously obtain information on both $2\theta/\theta$ and rocking curve ω. The measurement results will thus explicate the temperature (T) dependence of the implicate order during the solid-state-crystallization. Here, the implicate order characterized in polycrystalline films denotes both long-range lattice order within crystallites and alignment order between grains. We propose a temperature that characterizes the evolution of the implicate order, instead of the conventional

 © 2020 The Japan Society of Applied Physics

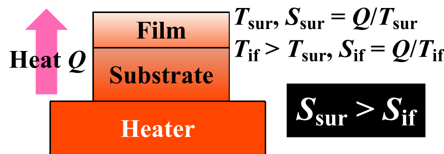

Fig. 1. (Color online) Schematic view of a generation of entropy within a film during flowing a heat Q from a heater. Note that non-equibrium process that shows the difference in temperatures between film surface and the interface between a film and substrate essentially causes entropy generation, resulting in the surface entropy (S_{sur}) larger than the interface one (S_{sur}).

T_{cr}, based on our analysis of the data concerning not only the grain growth but also the intercrystallite orientation obtained by the 2D-XRD measurement.

a-ITO films with a thickness of 50 nm were grown on non-alkali glass (Corning Eagle XG) substrates without intentionally heating the substrates, by reactive plasma deposition with direct-current arc discharge.[26–28] The source used was a sintered In_2O_3 pellet with a SnO_2 content of 5 wt% (corresponding to 4.6 at%). The deposition conditions are described in detail elsewhere.[26] The flow rate of oxygen (O_2) gas was 17 sccm.

In situ XRD measurements during solid-state crystallization were performed using Rigaku SmartLab. The *a*-ITO film sample was placed on a heating stage and heated from room temperature to 300 °C at a rate of 5.0 °C min^{-1}. The film was covered with a plastic dome having two pinholes to transmit X-ray beams. Cu-Kα1 X-ray with a wavelength of 0.154 05 nm was monochromated and parallelized by a curved mutilayer mirror and subsequently focused (to a cross sectional diameter of ∼1 mm on the sample) by Cross Beam Optics™. The diffracted X-ray was collected by a 2D high-speed detector (HyPix-3000). The angles of both the incident beam and the center of the detector with respect to the sample surface were fixed to 30°. The optical geometry is the same as that seen in Fig. 5 of Ref. 24. The $2\theta/\theta$ and ω curves were obtained by integrating the 2D profile along the ω and 2θ axes, respectively. Because of the size limit of the 2D detector and a long wavelength of conventional Cu-Kα Xray, we focused on a (222) diffraction with ranges of 2θ and ω of 22.5°–34.2° and ±30°, respectively. To estimate the lateral size of grains, in-plane XRD measurements were also carried out after the solid-state crystallization using the same machine at room temperature. In this case, the incident X-ray was not focused and its angle with respect to the surface of the film was fixed at 0.7°. The diffracted beam was collected using a conventional scintillation counter. The peak position and full-widths at half maximum (FWHMs) along the 2θ and ω axes corresponding to (222) diffraction, namely, $2\theta_{222}$, $\Delta(2\theta_{222})$, and $\Delta\omega$, respectively, were derived by the nonlinear fitting of a Gaussian distribution. The standard deviations of these parameters were calculated as square roots of diagonal components of a variance-covariance matrix. In addition, those of 2θ in-plane profiles were obtained by the same method. The grain size parallel and perpendicular to the surface of the film was calculated using the Scherrer formula[29] after subtracting the geometrical smearing.[30]

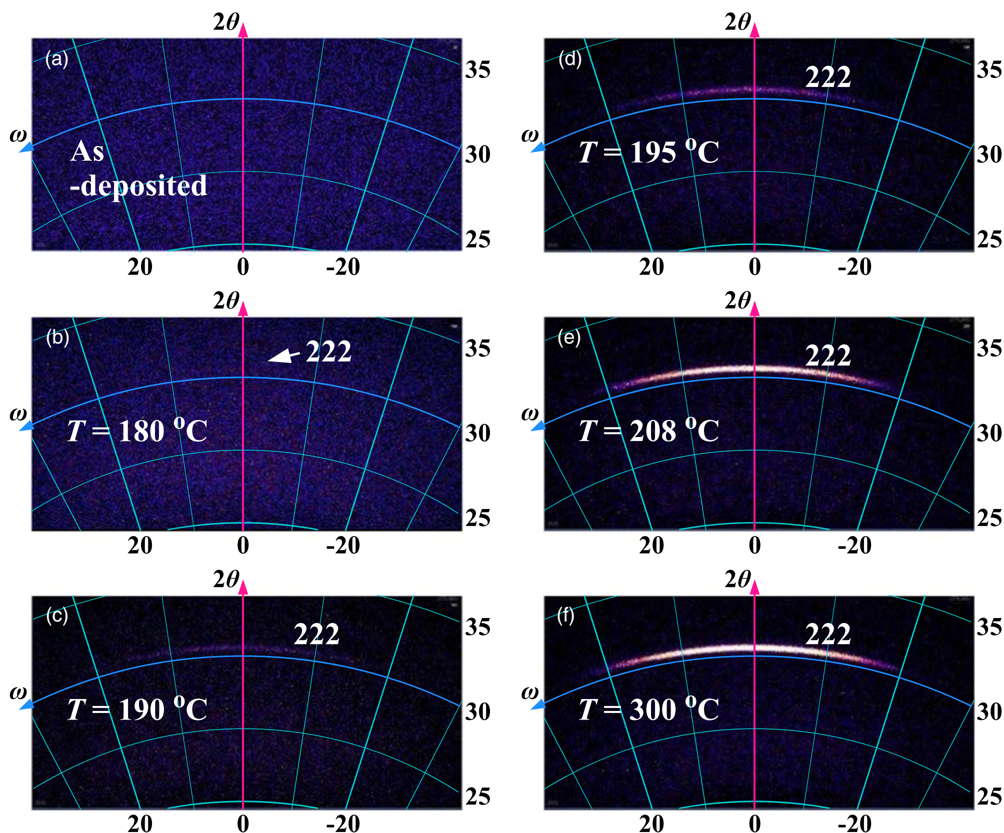

Fig. 2. (Color online) Two-dimensional XRD patterns near (222) diffraction for *a*-ITO film: (a) as-deposited, (b) just start of crystallization [peak could be detectable after an integration; stage [A] in Fig. 5], (c) halfway through grain orderings [stage [B] in Fig. 5], (d) start of dominant lateral crystallization [stage [C] in Fig. 5], (e) halfway thorough crystallization [stage [D] in Fig. 5], and (f) immediately after annealing at 300 °C.

© 2020 The Japan Society of Applied Physics

The electrical properties at room temperature were determined by Hall effect measurements in a van der Pauw geometry (Nanometrics HL5500PC).

Figure 2 shows the development of 2D XRD patterns for an *a*-ITO film with increasing *T*. Figure 2(a) shows that no signal was detected for the as-deposited *a*-ITO film. At approximately 180 °C, a (222) peak appeared suddenly [Fig. 2(b)]. At 190 °C, a slight signal was observed, as seen in Fig. 2(c), where the 2D XRD pattern exhibits a diffraction arc rather than fine spots, which indicates very weakly alignments between crystallites. When *T* reached 208 °C, a clear signal with retaining the diffraction arc was observed: The intensities are concentrated in an arc within the diffraction rings, indicating that a fraction of bixbyite crystallites has a preferential crystallographic orientation, as shown in Fig. 2(e). Upon further increasing *T* to 300 °C, the ITO film shows more intense patterns while retaining the diffraction arc.

Figure 3 shows the integrated intensity of the (222) peak (I_{222}), the *T* derivative of I_{222} (dI_{222}/dT), the grain size along the [222] axis perpendicular to the film surface (L_{222}), and the FWHM of the rocking curve ($\Delta\omega$) for the *a*-ITO film as functions of *T*. With increasing *T*, the increase in I_{222} is attributed to the increase in not only the degree of preferential crystal orientation but also crystallite growth along the (222) plane. Note that these *T*-dependences are time evolution and irreversible. Most parameters changed markedly near $T = 208$ °C, where dI_{222}/dT is maximum, above which they remained almost constant up to 300 °C; L_{222} and $\Delta\omega$ were 29.6 ± 0.2 nm and $24.6° \pm 0.2°$, respectively. The conventional one-dimensional $2\theta/\omega$ scan revealed that there was only an intense (222) peak after the heating. The (222) texture is expected since the close-packed (222) plane in the bixbyite structure has the highest density of atoms; the formation of (222) grains is energetically favorable. The structural parameters such as L_{222} and $\Delta\omega$, and lattice parameter *a*, which were determined by the XRD measurements at 300 °C, are summarized in Table I.

To estimate the lateral size of grains after the solid-state crystallization, the 2θ profile was obtained by in-plane XRD measurements at room temperature. The equivalent {440} peak was the most intense because of the perpendicular relationship between (222) and {440} planes. After the subtraction of geometrical smearing from the {440} peak, a lateral grain size L_{440} of 40.2 ± 1.5 nm, illustrated in Table I, which was larger than the corresponding vertical size L_{222}, was obtained.

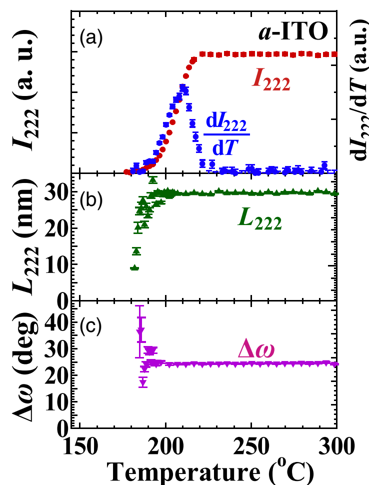

Fig. 3. (Color online) (a) Integrated intensity of (222) peak I_{222} (red circles), temperature derivative of I_{222} (dI_{222}/dT) (blue circles), (b) grain size L_{222}, and (c) FWHM of rocking curve $\Delta\omega$ for the *a*-ITO film as functions of temperature *T*.

Table I. $T_{cr,ss}$, T_{top}, L_{222}, $\Delta\omega$, *a*, L_{440}, ρ, n_e, μ_H, and λ_{MFP} of 50 nm thick postannealed ITO films.

$T_{cr,ss}$ (°C)	195.0(17)
T_{top} (°C)	208.5(2)
L_{222} (nm)	29.6(2)
$\Delta\omega$ (deg)	24.6(2)
a (nm)	1.014(0)
L_{440} (nm)	40.2(15)
ρ (Ω cm)	3.24×10^{-4}
n_e (cm^{-3})	4.44×10^{20}
μ_H (cm^2 V^{-1} s^{-1})	43.4
λ_{MFP} (nm)	6.74

The electrical properties of postannealed *a*-ITO at room temperature were determined by Hall effect measurements. The electrical resistivity ρ, carrier concentration n_e, and μ_H were 3.24×10^{-4} Ω cm, 4.44×10^{20} cm^{-3}, and 43.4 cm^2 V^{-1} s^{-1}, respectively. The corresponding mean free path of carriers (λ_{MFP}) based on the Fermi gas model[26] was 6.74 nm. The above electrical properties and λ_{MFP} are listed in Table I. The ratio of L_{440} to λ_{MFP} was calculated to be 5.9, which means that the carriers on average collide more than five times within a grain. This indicates that the electrical transport in the polycrystalline ITO film is not dominated by the scattering of grain boundaries.

In the following, we define a solid-state crystallization temperature $T_{cr,ss}$ relative to the evolution of the implicate order in *a*-ITO films on the basis of our analysis of the data concerning not only the growth of grains but also the crystallographic orientation between crystallites ($\Delta\omega$). The most important point is to eliminate any ambiguous factor. A schematic of the well-defined T_{top} is shown in Fig. 4 as below; T_{top} is the temperature where dI_{222}/dT is maximum.[22) On the other hand, $T_{cr,ss}$ is defined as the temperature at the intersection between the tangent to the I_{222} curve at $T = T_{top}$ and the baseline of I_{222}, corresponding to the peak intensity of fine crystallites at their initial occurrence. For the *a*-ITO film under investigation, the obtained T_{top} and $T_{cr,ss}$ were 208.5 °C ± 0.2 °C and 195.0°C ± 1.7 °C, respectively. The fundamental physical meaning of $T_{cr,ss}$ will be clearly elucidated below. We constructed a schematic view of the evolution of implicate order near $T_{cr,ss}$. Note that Fig. 3

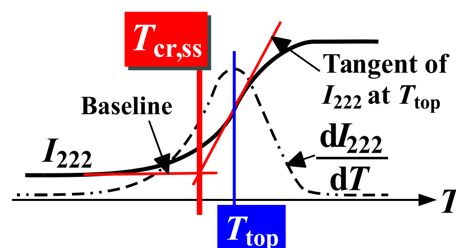

Fig. 4. (Color online) Schematic illustration of definitions of T_{top} and $T_{cr,ss}$ using plots of I_{222} and dI_{222}/dT.

© 2020 The Japan Society of Applied Physics

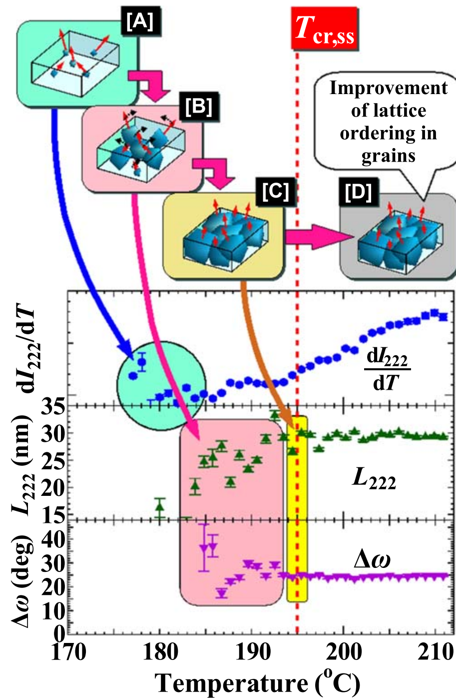

Fig. 5. (Color online) Possible formation mechanism of crystallized phase in *a*-ITO film: [A] nucleation, [B] competition between isotropic growth and improvement in intergrain orientation, [C] end of the grain growth and improvement of the orientation of crystallites, and [D] improvement of lattice ordering within grains. Red arrows represent crystal orientation of grains with respect to a film surface. T dependencies of dI_{222}/dT, L_{222}, and $\Delta\omega$ in the temperature range of crystallization are also shown. The crystallization temperature $T_{cr,ss}$ is shown as a vertical thick dotted line.

shows that both L_{222} and $\Delta\omega$ start to saturate at $T = T_{cr,ss}$, which is followed by little change up to 300 °C. This indicates that the remaining evolution of implicate order involves the linking of InO_6 octahedra, giving an ordered array.

A schematic diagram of the phenomena occurring during the solid-state crystallization process is shown in Fig. 5. The process is composed of some stages. In the temperature range from around 180 °C to $T_{cr,ss}$, a first-stage-orientation would arise during nucleation, [A] as shown in Fig. 5, after the onset of further crystallite growth, where space and time no longer seem to be the dominant factors that determine the dependence or independence of different crystallites; subsequently, impingement and coalescence of crystallites, [B] as shown in Fig. 5, where we find the competition between isotropic growth of the grains together with in-grain lattice ordering and alignment between the crystallites. Taking into account of the discussion as shown in Fig. 1, non-equilibrium process in this study suppresses the improvement in the crystallographic orientation between the grains. Note that the critical temperature range from 187 °C to $T_{cr,ss}$ in the first-stage-orientation; with elevating T, the magnitude of $\Delta\omega$ tend to increase. When T reaches $T_{cr,ss}$, the intergrain ordering and grain growth were almost finished [[C] in Fig. 5]. At the final stage, followed by $T = T_{cr,ss}$, a continuous increase in dI_{222}/dT and I_{222} shows an improvement of lattice ordering within grains [[D] in Fig. 5], which could be explained in terms of a conventional phenomena of lattice ordering in single crystallite films. The above finding shows that $T_{cr,ss}$ is the starting point of the lattice ordering in grains as well the end point of the intergrain ordering together with the growth of grains. As a well-defined crystallization temperature for polycrystalline ITO films prepared by the non-equilibrium solid-state crystallization method, therefore, we propose a temperature at which the above-mentioned final stage starts.

In conclusion, the 2D XRD technique used to obtain the T dependence of diffraction patterns for 50 nm thick *a*-ITO films is effective for elucidating the evolution of implicate order, i.e., long-range lattice order in grains together with the alignment between crystallites during postannealing solid-state crystallization. We concluded that $T_{cr,ss}$ is eminently suitable as a well-defined solid-state-crystallization temperature for polycrystallization ITO films prepared under a non-equibrium environment. Investigating dominant factors that determine $T_{cr,ss}$ and elucidating a relationship between $T_{cr,ss}$ and film properties will be essential for achieving advanced ITO films showing a high μ_H and optical transparency. The difference in $T_{cr,ss}$ of ITO films between prepared by the conditions of equilibrium at a very low heating rate and of non-equilibrium at a high one must be studied in near future. The elucidation of the dynamics of the solid-state crystallization accompanying the competition between the grain growth and the alignment between crystallites is essential for achieving advanced functional oxides.

This study was supported by a collaboration with Sumitomo Heavy Industries, Ltd. [Patent: WO2017/014278A1 (Sumitomo Heavy Industries, Ltd.), 2017-01-26].

1) G. L. Olson and J. A. Roth, Mater. Sci. Rep. **3**, 1 (1988).
2) S. Y. Yoon, S. J. Park, K. H. Kim, and J. Jang, Thin Solid Films **383**, 34 (2001).
3) N. Kaiser, Thin Solid Films **116**, 259 (1984).
4) K. Lu, Mater. Sci. Eng. **R16**, 161 (1996).
5) J. R. Bosnell and U. C. Voisey, Thin Solid Films **6**, 161 (1970).
6) K. Yanagisawa and J. Ovenstone, J. Phys. Chem. B **103**, 7781 (1999).
7) H. Zhang and J. F. Banfield, Chem. Mater. **14**, 4145 (2002).
8) E. Kobayashi, Y. Watabe, and T. Yamamoto, Appl. Phys. Express **8**, 015505 (2015).
9) D. S. Ginley and C. Bright, MRS Bull. **25**, 15 (2000).
10) I. Hamberg and C. G. Granqvist, J. Appl. Phys. **60**, R123 (1986).
11) S. Calnan and A. N. Tiwari, Thin Solid Films **518**, 1839 (2010).
12) M. Lorenz, M. R. Rao, T. Venkatesan, E. Fortunato, P. Barquinha, R. Branquinho, D. Salgueiro, R. Martins, E. Carlos, and A. Liu, J. Phys. D **49**, 433001 (2016).
13) T. Koida, Y. Ueno, and H. Shibata, Phys. Status Solidi A **215**, 1700506 (2018).
14) F. O. Adurodija, L. Semple, and R. Brüning, J. Mater. Sci. **41**, 7096 (2006).
15) M. Ando, E. Nishimura, K. Onisawa, and T. Minemura, J. Appl. Phys. **93**, 1032 (2003).
16) Y. Hu, X. Diao, C. Wang, W. Hao, and T. Wang, Vacuum **75**, 183 (2004).
17) D. C. Paine, T. Whitson, D. Janiac, R. Beresford, C. O. Yang, and B. Lewis, J. Appl. Phys. **85**, 8445 (1999).
18) P. K. Song, H. Akao, M. Kamei, Y. Shigesato, and I. Yasui, Jpn. J. Appl. Phys. **38**, 5224 (1999).
19) M. Avrami, J. Chem. Phys. **7**, 1103 (1939).
20) X.-Q. Yang, J. McBreen, W.-S. Yoon, and C. P. Grey, Electrochem. Commun. **4**, 649 (2002).
21) M. Azuma, H. Yoshida, T. Saito, T. Yamada, and M. Takano, J. Am. Chem. Soc. **126**, 8244 (2004).
22) W. Knaepen, C. Detavernier, R. L. Van Meirhaeghe, J. J. Sweet, and C. Lavoie, Thin Solid Films **516**, 4946 (2008).
23) S. Kobayashi and K. Inaba, Rigaku J. **28**, 8 (2012).
24) K. Inaba, S. Kobayashi, K. Uehara, A. Okada, S. L. Reddy, and T. Endo, Adv. Mater. Phys. Chem. **3**, 72 (2013).

© 2020 The Japan Society of Applied Physics

25) L. Zeng, M. M. Moghadam, D. B. Buchholz, R. Li, D. T. Keane, V. P. Dravid, R. P. H. Chang, P. W. Voorhees, T. J. Marks, and M. J. Bedzyk, Phys. Rev. Mater. **2**, 053401 (2018).
26) Y. Furubayashi, M. Maehara, and T. Yamamoto, Nanoscale Res. Lett. **14**, 120 (2019).
27) Y. Furubayashi, M. Maehara, and T. Yamamoto, ACS Appl. Electron. Mater. **1**, 1545 (2019).
28) T. Yamamoto, H. Song, and H. Makino, Phys. Status Solidi C **10**, 603 (2013).
29) A. L. Patterson, Phys. Rev. **56**, 978 (1939).
30) L. Zeng, M. M. Moghadam, D. B. Buchholz, R. Li, D. T. Keane, V. P. Dravid, R. P. H. Chang, P. W. Voorhees, T. J. Marks, and M. J. Bedzyk, *Supplemental Material of Processing-Dependent Thermal Stability of a Prototypical Amorphous Metal Oxide* [http://link.aps.org/supplemental/10.1103/PhysRevMaterials.2.053401].

 © 2020 The Japan Society of Applied Physics